BIOL S4503 Supervised Research Final Report

Tumor Treatment Investigation through Imaging of Mouse Brain

Nanyan Zhu[1]

Mentor: Andrew F. Laine[2]

Supervisor: Jia Guo[3]

[1]Master Student, Department of Biological Science, Columbia University, New York, NY

[2]Percy K. & Vida L. W. Hudson Professor, Biomedical Engineering Department, Columbia University, New York, NY

[3]Assistant Professor of Neurobiology, Psychiatry Department, Columbia University, New York, NY

PROJECT OBJECTIVE

We quantitatively evaluated the effectiveness of using the drug Etoposide to treat Glioblastoma in mice. For these purposes, we designed and implemented a novel scan protocol, dynamic T2-relaxation contrast (DRC), to generate cerebral blood volume, cerebral blood flow and other quantitative mappings of the mice brain hemodynamics.

I. Introduction

Glioblastoma (GBM) is the most common and most lethal brain tumor [1]. With its remarkable aggressiveness, GBM cells tend to spread extensively in the brain parenchyma and most patients diagnosed with GBM lose their lives within a year [2]. Multiple research teams worldwide spent huge efforts on potential treatments of this notorious disease, but no cure has yet been found. For instance, [3] investigated the possibility of blocking the PI3K signaling pathway with pharmacological inhibitors, [4] demonstrated that combination treatment with AdFlt3L and AdTK is effective for GBM, and [5] showed that systemic administration of TG6002 inhibits the growth

of a human GBM cell line implanted in mice. By far, Etoposide administration seems to be one of the most promising chemotherapeutics as one of the TOP2 targeting Drugs [6][7][8][28], but to the best of our knowledge none of the previous studies had focused on *in vivo* evaluation of the treatment, with part of the reason being the lack of an imaging modality that is capable of reflecting brain metabolism and function at a high spatial resolution.

Brain metabolism and function can be depicted by cerebral perfusion hemodynamics using non-invasive magnetic resonance imaging (MRI). Hemodynamics mappings such as cerebral blood flow (CBF) and cerebral blood volume (CBV) are widely used in preclinical applications using transgenic mouse models, including the classification of tumors [9], identification of stroke [10], and characterization of other brain dysfunctions [11][12][13]. The biggest challenge still lies in the imaging resolution: the millimeter-scale resolution of most MRI applications is suboptimal, if not unacceptable, for *in vivo* inspection of tumor treatments.

Thanks to the recent advances in MRI hardware, our lab is equipped with a Bruker Biospec 94/30 scanner at 9.4 T with CryoProbe technology [14], which enables micrometer-scale resolution and eventually meets the aforementioned requirements. In this paper we will quantify the treatment effectiveness of Etoposide on Glioblastoma in mice brain via multiple hemodynamics mappings using a novel modeling method based on T2-weighted MRI.

II. Subjects and Methods

A. Animal Subjects and Experimental Design

(i) Animal Subjects

The animal subjects used in our study are 4 adult male mice of C576J/BL genotype.

(ii) Experimental Groups

The 4 mice were randomly assigned to the treatment and control groups so that each group consisted of 2 subjects. PDGFB(+/+) PTEN(-/-) p53(-/-) Glioblastoma cells were administered into the brains of all 4 mice in both experimental groups via injection. 5,000 cells, with a total volume of 1 μL, were stereotactically injected into the brains.

After that, in the treatment group, Etoposide was intraperitoneally (IP) injected into the mice at a dosage of 40 mg/kg body weight 7 and 14 days after tumor implantation. No injection was provided to the control group.

T2-weighted MRI scans with IP-injected Gadodiamide as the contrast agent (CA) were acquired for all subjects at 10, 14, and 21 days after the initial treatment, or in other words, 17, 21, and 28 days after tumor implantation. The GBM treatment effects were later quantified by cerebral perfusion dynamics mappings, including the aforementioned CBV, CBF, and two additional quantitative metrics: mean transit time (MTT) and wash-in rate (WIR).

B. Method for Cerebral Hemodynamics Modeling

A commonly-used method to obtain hemodynamic mappings is dynamic susceptibility contrast MRI (DSC-MRI) [15]. However, it has two major shortcomings that rendered it non-ideal for our application: it is "limited by low resolution and distortion" as stated in [16]; moreover, it requires intravenous (IV) injection of CA which is difficult to carry out in mice [17]. Steady-state imaging methods, such as steady-state contrast-enhanced MRI (SSCE-MRI), boost the spatial resolution but are only viable for certain hemodynamics mappings (e.g., CBV) but not others. To resolve these challenges, we implemented our new method called dynamic T2-relaxation contrast MRI (DRC-MRI), which allows the modeling of all required hemodynamics mappings with the IP injection of CA.

C. Data Acquisition

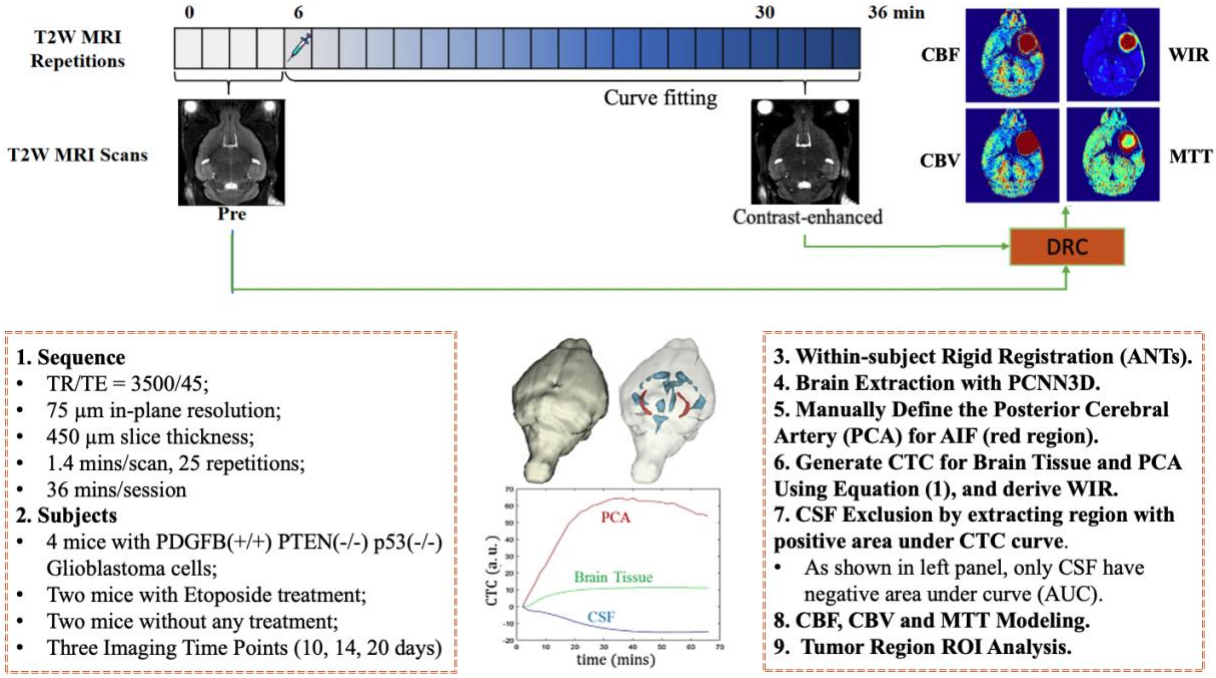

Figure 1. Overview of the data acquisition process and the proposed DRC pipeline.

(i) Functional MRI (fMRI)

For the mouse study, scans were acquired using CBV-fMRI protocols as described in [12] [17] [18]. A Bruker BioSpec 94/30 (field strength, 9.4 T; bore size, 30 cm) horizontal small animal MRI scanner with software ParaVision 6.0.1 (Bruker BioSpin, Billerica, MA, USA), an 86-mm inner diameter birdcage 1H volume transmit coil and a 1H Cryo-probe mouse head 2x2 surface array receive coil will be used for the imaging. Mice were anesthetized using the medical air and isoflurane (3% volume for induction, 1.1-1.5% for maintenance at 1 liter/min aiflow, via a nose cone). A flowing water heating pad was used to maintain body temperature at around 37°C. Sterile eye lubricant was applied after each scan. Twenty-five T2-weighted anatomical brain scans were

dynamically acquired before and during the IP injections of the contrast agent Gadodiamide (Omniscan; GE Healthcare, Princeton, NJ, USA) at the dosage of 10 mmol/kg for CBV and CBF mapping [18]. T2-weighted scans were acquired with a fast-spin echo acquisition (TR = 3500 ms, effective TE = 45 ms, RARE factor = 8, FOV = 15.1 × 15.1 × 8.1 mm^3, voxel size = 75 × 75 × 450 μm^3, number of repetitions = 25).

(ii) Structural MRI (sMRI)

sMRI scans were derived from the fMRI data. For each mouse, T2-weighted scans from the same contrast-enhanced dynamic scan were intensity-normalized, skull-stripped [19] and linearly co-registered [20].

D. Cerebral Hemodynamics Modeling

This section demonstrates how to quantify cerebral hemodynamics using the DRC-MRI method. Quantitative modeling of DRC mapping combining features of dynamic and steady-state methods is simulated. CBF was quantified based on the deconvolution model with tissue residue function analyzed in a similar way as the DSC-MRI. Figure.2A-B represent simulated AIF and CTC we typically observed in the DSC study, and Fig2.C is the CBF-scaled TRF, CBF·R, calculated using Equation (4) with SVD-deconvolution. We approximate the $\widehat{AIF}$ observed in the DRC experiment (Fig.2G) as a

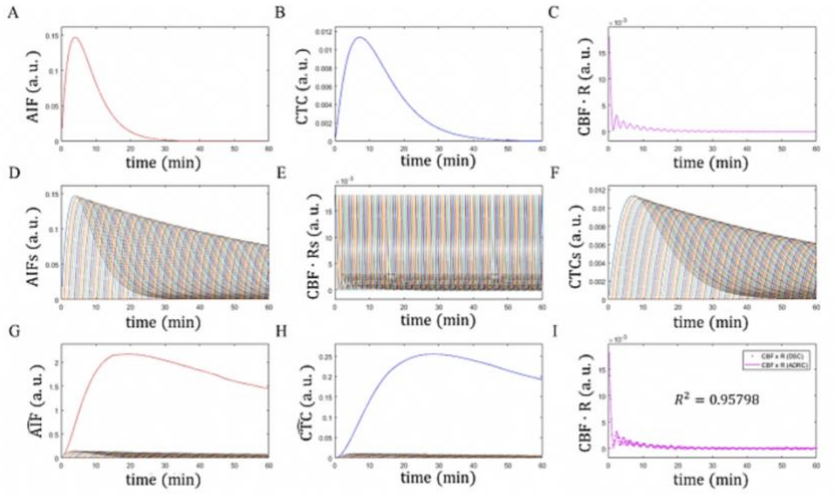

Figure 2. Modeling CBF of simulated dataset using the deconvolution method.

summation of 100 time-shifted mono-exponentially decaying fast bolus pass AIFs (Fig.2D). The CBV was quantified in a similar way as the SSCE-MRI, and the method will be illustrated as follows. With the CBF·R calculated ready, the $\widehat{CTC}$ observed in the DRC experiment is calculated using Equation (10) by first convolving each individual *AIF(t-i·Δt)* (Fig.2D) with the corresponding CBF-scaled TRF *CBF·R (t-i·Δt)* (Fig.2E) to obtain *CTC(t-i·Δt)* (Fig.2F). and then summing them together to derive $\widehat{CTC}$ (Fig.2H). The two remaining mappings were derived using the normal standards.

(i) DRC Modeling

After within-subject rigid registration of all MR scans from the 25 repetitions using ANTs [21], brain extractions were performed with PCNN3D [19]. The first step of modeling the DRC data is to convert the T2 signal-time-course of each voxel into a curve that represents the concentration of the CA in the brain tissue, known as the concentration-time-course (CTC). As T1 effects are neglectable in the tissue when TR > 3 × T1, using the SE-EPI sequence with TR = 3000 ms, the CA concentration can be approximated using the following equation,

$$C(t) = \frac{\Delta R_2}{r_{tissue}} = \frac{1}{r_{tissue} \cdot TE} \ln\left(\frac{S(0)}{S(t)}\right) \quad (1)$$

where the CA concentration is proportional to the changes in the relaxation rate R_2, constant r_{tissue} is assumed to be the same for the whole brain [22].

(ii) CBF Modeling

In DSC-MRI, rCBF is estimated using the mathematical technique of deconvolution with the principle of indicator dilution theory [23] by solving the following equation,

$$CTC(t) = (CBF \cdot R(t)) \otimes AIF(t) \quad (2)$$

where arterial input function AIF(t) is the arterial CTC and R(t) is the tissue residue function (TRF), which describes the retention of contrast agent within the capillary bed. The quantification

of CBF requires the inversion of Equation (2), which can be expressed in vector-matrix notations below,

$$\boldsymbol{AIF} \cdot (CBF \cdot \boldsymbol{R}) = \boldsymbol{CTC} \tag{3}$$

$$CBF \cdot \boldsymbol{R} = \boldsymbol{AIF}^{+} \cdot \boldsymbol{CTC} \tag{4}$$

$$CBF = \max[CBF \cdot \boldsymbol{R}] \tag{5}$$

where column vector $[CBF \cdot R]$ contains the unknown discrete CBF-scaled TRF and the matrix AIF has elements:

$$a_{i,j} = \begin{cases} \Delta t \cdot AIF(t - i \cdot \Delta t) & j \leq i \\ 0 & j > i \end{cases} \tag{6}$$

where $\boldsymbol{AIF}$ can be up-sampled with interpolation (i.e., we used the smooth spline algorithm). And the pseudoinverse of $\boldsymbol{AIF}$, $\boldsymbol{AIF}^{+}$, is calculated using singular value decomposition (SVD). A regularization cut-off of $P_{SVD} = 20\%$ is used to remove the singular values and reduce the effects of noise as suggested in [24].

Here we show that DRC can map CBF using the deconvolution method. By observing our *in vivo* data carefully, we hypothesize that the AIF of the DRC experiment, $\widehat{AIF}$ (Fig. 2G) can be approximated as the summation of a train of independent time-shifted fast-pass $AIFs$ (Figure. 2D) as shown in Equation (7). And we assume those N time-shifted fast-pass $AIFs$ have a mono-exponentially decaying factor α, since eventually there is no CA left in the artery. Each fast-pass $AIF(t)$ (Figure. 2A) used in Equation (7) can be modeled with a Gamma function which is typically used in DSC [25].

$$\widehat{AIF}(t) = \sum_{i=1}^{N} \alpha(i) \cdot AIF(t - i \cdot \Delta t) \tag{7}$$

$$\alpha(i) = 1 \cdot \exp\left(-a \cdot \frac{i}{N}\right) \tag{8}$$

For each $(\alpha(i) \cdot AIF(t - i \cdot \Delta t))$ in Equation (7), we can express its corresponding $CTC(t - i \cdot \Delta t)$ using Equation (2),

$$CTC(t - i \cdot \Delta t) = \big(CBF \cdot R(t - i \cdot \Delta t)\big) \otimes (\alpha(i) \cdot AIF(t - i \cdot \Delta t)) \tag{9}$$

So that the $\widehat{CTC}(t)$ (Figure. 2H) observed with IP injection can be expressed as the summation of all $CTC(t - i \cdot \Delta t)$ (Figure. 2F),

$$\begin{aligned}
\widehat{CTC}(t) &= \sum_{i=1}^{N} CTC(t - i \cdot \Delta t) \\
&= \sum_{i=1}^{N} \big(CBF \cdot R(t - i \cdot \Delta t)\big) \otimes \big(\alpha(i) \cdot AIF(t - i \cdot \Delta t)\big) \\
&= \sum_{i=1}^{N} \big(CBF \cdot R(t)\big) \otimes \big(\alpha(i) \cdot AIF(t - i \cdot \Delta t)\big) \otimes \delta(t - i \cdot \Delta t) \\
&= \big(CBF \cdot R(t)\big) \otimes \left(\sum_{i=1}^{N} \big(\alpha(i) \cdot AIF(t - i \cdot \Delta t)\big) \right)
\end{aligned} \tag{10}$$

which gives,

$$\widehat{CTC}(t) = \big(CBF \cdot R(t)\big) \otimes \widehat{AIF}(t) \tag{11}$$

and can be written in vector-matrix forms,

$$\boldsymbol{\widehat{AIF}} \cdot (CBF \cdot \boldsymbol{R}) = \boldsymbol{\widehat{CTC}} \tag{12}$$

so that,

$$CBF \cdot \boldsymbol{R} = \boldsymbol{\widehat{AIF}^{+}} \cdot \boldsymbol{\widehat{CTC}} \tag{13}$$

$$CBF = \max[CBF \cdot \boldsymbol{R}] \tag{14}$$

Comparing Equation (11-14) with Equation (2-5), we prove that DRC can map CBF in the same way as DSC using the deconvolution method (Figure. 2I). Further validations were performed on both simulated and *in vivo* experimental data.

For absolute quantification of CBF, the multiplication of CBF by the Hct correction factor k_H is required. In practice, k_H is set to 0.733 [26]. Finally, CBF was normalized by the estimated mean value in the PCA region to obtain the relative CBF (rCBF).

(iii) CBV Modeling

Similar to SSCE-MRI, CBV can be modeled as the blood volume fraction (BVf) as following,

$$CBV = \frac{k_H}{\rho} BVf = \frac{k_H}{\rho} \frac{CTC_{ss}}{AIF_{ss}} = \frac{k_H}{\rho} \frac{C_{max}}{A_{max}} \tag{15}$$

where CTC_{ss} represents the steady-state CA concentration in the brain tissue (when T2 signal reaches the plateau phase), and AIF_{ss} is associated with the artery. With IP, the plateau phase also has the highest CA concentration for both brain tissue and AIF. Considering an easy and robust implementation, CTC_{ss} and AIF_{SS} are replaced with C_{max} and A_{max} (Figure. 3A-B), respectively. For absolute quantification of CBV, Hct correction factor k_H and brain tissue density ρ are necessary. In practice, ρ is set to 1.0 g/mL [25]. Finally, CBV was normalized by the estimated mean value in the PCA region to obtain the relative CBV (rCBV).

(iv) MTT Modeling

MTT represents the time the blood (represented by the CA) spends in the capillary bed, which is calculated as the ratio between CBV and CBF using the central volume theorem [23],

$$MTT = \frac{CBV}{CBF} \tag{16}$$

(v) WIR Modeling

WIR indicates the rate at which the tissues absorb the CA, which can be modeled as the derivative of CTC with respect to time,

$$WIR = \frac{d\ CTC}{dt} \tag{17}$$

E. Tumor Region Analysis

(i) GBM Differentiation by Multivariate K-means

In order to quantitatively evaluate the treatment effect, we performed tumor segmentation and detailed tumor-region statistical analysis. The tumor segmentation was done by a multivariate K-means clustering on the WIR and rCBV mappings. Since intensity ranges of different brain tissues are distinct by nature, voxels in the scans automatically aggregated into 4 clusters corresponding to gray matter, white matter, cerebral spinal fluid and background, and tumor. The tumor cluster was then identified and subsequent image closing, hole-filling as well as dilation were applied to refine the segmentation.

(ii) Quantitative Tumor Region Analysis

Quantitative tumor region analysis could thus be completed based on the rCBV, rCBF and WIR voxel values mean inside the tumor region.

III. Results

A. DRC Curve Fitting

The validity of our proposed DRC method is well supported by the fact that *in vivo* data in Figure 3 showed similar patterns of AIF, CTC and CBF * R as the simulated dataset. *In vivo* CA CTC was up-sampled 5.5 times with the smooth spline curve fitting for better demonstration.

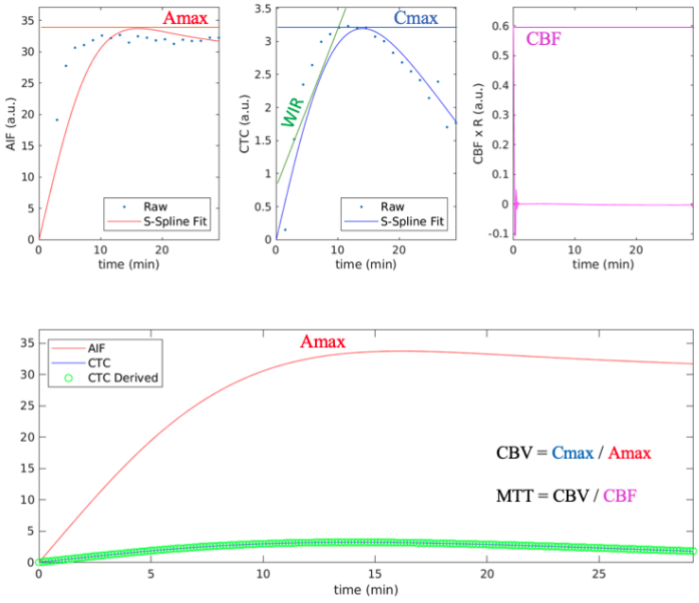

Figure 3. Modeling perfusion hemodynamics of *in vivo* data.
A-C. CBF Modeling. In panel B, the green line is the wash-in rate (WIR), which is mathematically equal to the derivative of CTC with respect to time. D. CBV and MTT Modeling.

B. Qualitative Analysis

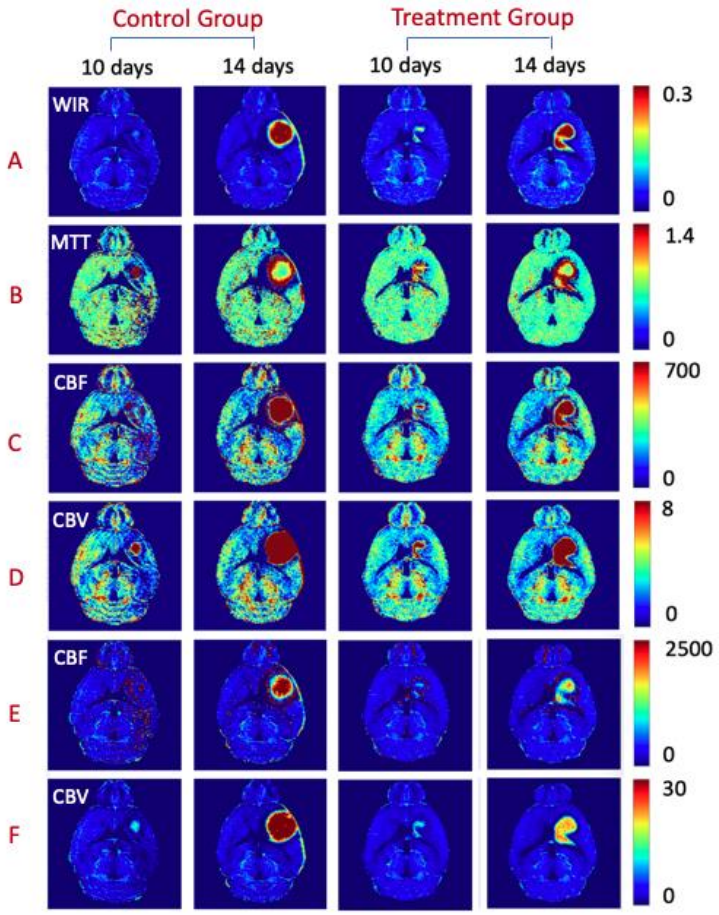

Figure 4. All cerebral hemodynamics mappings of one sample subject from each experimental group. The obtrusive objects, red colored in most mappings and breaks symmetricity, are the Glioblastomas. A. Wash-in rate (WIR). B. Mean transit time (MTT). C & E. Cerebral blood flow (CBF). D & F. Cerebral blood volume (CBV). For C-F, the intensity range for display are adjusted such that C-D highlight the non-tumor region and E-F highlight the tumor region.

As shown in Figure 4, the progression of GBM cells in the treatment group is significantly slower than the ones in the control group. By nature, tumor tissues have higher rCBV, rCBF, MTT and WIR than normal brain tissues, and therefore they can be easily distinguished in these hemodynamics mappings. The difference between control and treatment group is not very obvious on 10 days after initial treatment. However, 14 days after initial treatment, tumors in the control group become significantly larger (Figure 4. A-D). By observing Figure 4. E-F, where the display scales were adjusted to better visualize the tumor regions, we can conclude that the tumor-region rCBV and rCBF values are also lower than those of the control group. These qualitative results suggest that Etoposide treatments suppressed the spreading of Glioblastoma cells.

More notably, both mice in the control group have dead the third week after initial treatment (and thus we did not acquire the third set of scans as planned on day 20), but the mice in the treatment group were still alive. This indicates that Etoposide treatment increased the median overall survival

(mOS), which means the length of time from starting treatment for GBM in mice that half of the mice in a group are still alive.

C. Quantitative Analysis

(i) Tumor Size

As shown in Figure 5A, the untreated tumor is bigger than the treated tumor based on the scan acquired 14 days after initial treatment. As shown in Figure 5B-C, within each experimental group, the tumor size increased by time, but the tumor growth in the treatment group was slower than in the control group.

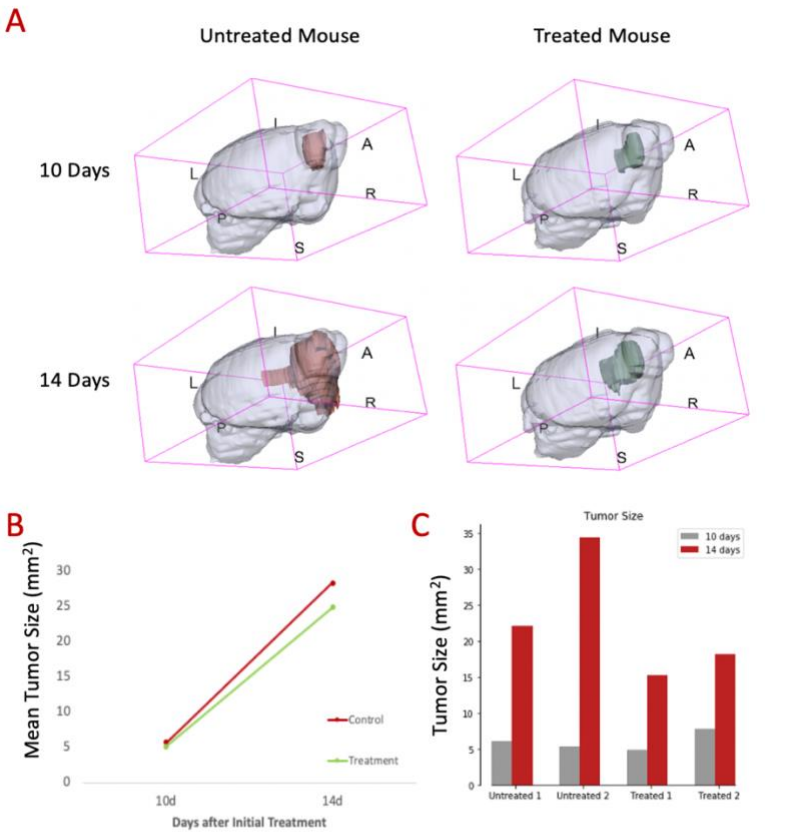

Figure 5. Comparison of Glioblastoma size with and without Etoposide treatment. A. Volume rendering of two sample mice brains, one from each experimental group, with tumor regions highlighted. B. Average tumor size within each experimental group. C. Tumor size by each individual subject.

(ii) Tumor Region rCBF, rCBV and WIR

In Figure 6A, the tumor regions were highlighted and the color scales within those regions represented the rCBV values. The difference in intensities and sizes of the tumor regions of treated and untreated mice both suggested the efficacy of Etoposide as an effective drug to suppress the tumor progression in mice. The treatment group has significantly lower tumor-region normalized CBF than that of the control group 10 days after the initial treatment, while no significant difference was found on normalized CBV, WIR and tumor size at that time (Figure 6B-G). As for the scans acquired 14 days after initial treatment, all three features (rCBF, rCBV, WIR) implied

slower tumor growth in the treatment group, and rCBV seemed to be the most differentiable feature among the three, which matched the conclusions of Neska-Matuszewska's team [27]. Although not all features being compared were the same between their study and ours, we collectively agreed that rCBV is the most sensitive to GBM progression. All these results indicated that the Etoposide treatment suppressed GBM progression in mice.

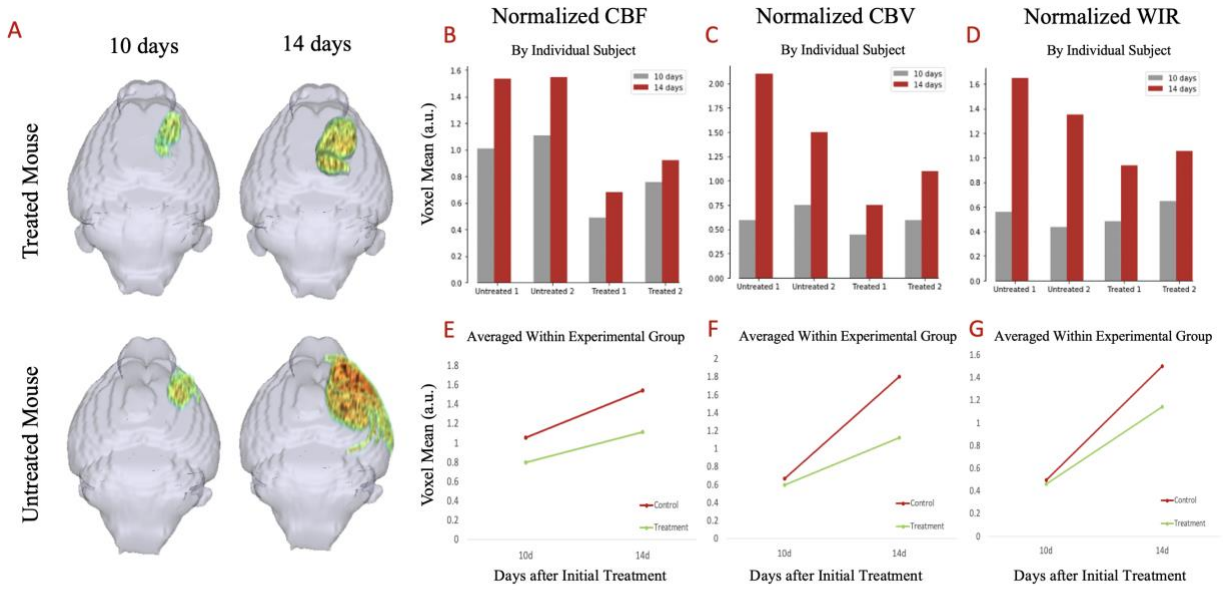

Figure 6. Comparison of Glioblastoma tumor-region statistics with and without Etoposide treatment.
A. Volume rendering of two sample mice brains, one from each experimental group, with tumor regions highlighted. B - G. Quantitative measures of cerebral blood flow (CBF), cerebral blood volume (CBV) and wash-in rate (WIR). B – D show the results by each individual subject, and E - G show the group average within each experimental group.

IV. Discussion

Our study suggested that Etoposide is effective in restricting the proliferation of Glioblastoma cells in mice brains, both in terms of tumor size and in terms of the level of abnormality in hemodynamics. We also confirmed that relative cerebral blood volume was the most sensitive to Glioblastoma proliferation among all hemodynamics features we compared. It took 2 weeks for the drug to take significant effect, and we believe that it is probably due to the fact that Etoposide cannot penetrate the blood-brain barrier (BBB) [28]. Etoposide had limited access to Glioblastoma cells until the latter deteriorated and destroyed the BBB, allowing the former to flow into the brain.

Although the experimental result is already satisfying, there exist three major areas of improvement in our study design and implementation. The first is the imperfection of CTC curve fitting. The curve fitting process assumed that the contrast agent concentration over time follows a beta function when increasing, then decreases. In other words, the concentration gradually peaks, saturates, and slowly dropped to a lower level. The peak CTC over the time course was used for CBV and CBF modeling. It has been observed that for a few scans the concentration level kept increasing even at the last repetition, and therefore the peak was likely underestimated for these scans, yielding inaccurate CBV and CBF estimations. To resolve this issue, additional repetitions and a consequently longer scan time will probably be necessary.

The second is the generalizability of the results in this study to other Glioblastoma cell subtypes. The molecular profile of Glioblastoma is diverse, and Etoposide may not be as effective on other Glioblastoma subtypes. As a TOP2 drug, it is reasonable that Etoposide can target the PDGFB(+/+) PTEN(-/-) p53(-/-) Glioblastoma, a subtype which highly expresses TOP2A and TOP2B [28], while its effect on other subtypes remain unclear and further verification will be necessary.

The third is the imperfect tumor-region segmentation. A multivariate K-means clustering followed by simple image closing, hole-filling and dilation successfully localize the tumor region but failed to generate segmentation with highly accurate boundaries. More sophisticated methods such as the Markov random field may be applied to refine the segmentation.

Beyond those, our study can also be pushed to the next level if further efforts are made in the identification of imaging biomarkers associated with Glioblastoma using high-resolution MRI. Our study also presented the possibility of applying the imaging protocol on evaluations of other drugs and diseases.

References

[1] Brem, S. & Abdullah, K. *Glioblastoma*. (Elsevier, 2017).

[2] Gallego, O. Nonsurgical treatment of recurrent glioblastoma. *Current Oncology* **22**, 273 (2015).

[3] Zhao, H-F., Wang, J., Shao, W., Wu, C-P., Chen, Z-P., To, S-S. & Li, W-P. Recent advances in the use of PI3K inhibitors for glioblastoma multiforme: current preclinical and clinical development. *Molecular Cancer* **16**, (2017).

[4] King, G., Muhammad, G., Curtin, J., Barcia, C., Puntel, M., Liu, C., Honig, S., Candolfi, M., Mondkar, S., Lowenstein, P. & CastroGene, M. Eradication of Multifocal Glioma in a Syngeneic Glioblastoma Multiforme with Ad-Flt3L and Ad-HSV1-TK. *Molecular Therapy* **15**, (2007).

[5] Idbaih, A., Erbs, P., Foloppe, J., Chneiweiss, H., Kempf, J., Homerin, M., Schmitt, C., Them, L. & Delattre, J-Y. TG6002: A novel oncolytic and vectorized gene pro-drug therapy approach to treat glioblastoma. *Journal of Clinical Oncology* **35**, (2017).

[6] Kuo, Y-C. & Wang, I-H. Using catanionic solid lipid nanoparticles with wheat germ agglutinin and lactoferrin for targeted delivery of etoposide to glioblastoma multiforme. *Journal of the Taiwan Institute of Chemical Engineers* **77**, 73–82 (2017).

[7] Sevim, H., Parkinson, J. & McDonald, K. Etoposide-mediated glioblastoma cell death: dependent or independent on the expression of its target, topoisomerase II alpha? *Journal of Cancer Research and Clinical Oncology* **137**, 1705–1712 (2011).

[8] Kuo, Y-C., Chang, Y-H. & Rajesh, R. Targeted delivery of etoposide, carmustine and doxorubicin to human glioblastoma cells using methoxy poly(ethylene glycol)-poly(ε-caprolactone) nanoparticles conjugated with wheat germ agglutinin and folic acid. *Materials Science and Engineering: C* **96**, 114–128 (2019).

[9] Borges, A., Lopez-Larrubia, P., Marques, J. & Cerdan, S. MR Imaging Features of High-Grade Gliomas in Murine Models: How They Compare with Human Disease, Reflect Tumor Biology, and Play a Role in Preclinical Trials. *American Journal of Neuroradiology* **33**, 24–36 (2012)

[10] Shen, Q. & Duong, T. Magnetic resonance imaging of cerebral blood flow in animal stroke models. *Brain Circulation* **2**, 20-27 (2016).

[11] Lewandowski, N., Bordelon, Y., Brickman, A., Angulo, S., Khan, U., Muraskin, J., Griffith, E., Wasserman, P., Menalled, L., Vonsattel, J., Marder, K., Small, S. & Moreno, H. Regional vulnerability in Huntington's disease: fMRI-guided molecular analysis in patients and a mouse model of disease. *Neurobiology of Disease* **52**, 84–93 (2013).

[12] Khan, U., Liu, L., Provenzano, F., Berman, D., Profaci, C., Sloan, R., Mayeux, R., Duff, K. & Small, S. Molecular drivers and cortical spread of lateral entorhinal cortex dysfunction in preclinical Alzheimer's disease. *Nature Neuroscience*; New York **17**, 304–11 (2014).

[13] Schobel, S., Chaudhury, N., Khan, U., Paniagua, B., Styner, M., Asllani, I., Inbar, B., Corcoran, C., Lieberman, J., Moore, H. & Small, S. Imaging Patients with Psychosis and a Mouse Model Establishes a Spreading Pattern of Hippocampal Dysfunction and Implicates Glutamate as a Driver. *Neuron* **78**, 81–93 (2013).

[14] Bruker BioSpins MRI CryoProbe™. *Materials Today* **11**, 60 (2008).

[15] López-Larrubia, P. Dynamic Susceptibility Contrast MRI in Small Animals. Preclinical MRI Methods in *Molecular Biology* 41–57 (2018).

[16] Varallyay, C., Nesbit, E., Fu, R., Gahramanov, S., Moloney, B., Earl, E., Muldoon, L., Li, X., Rooney, W. & Neuwelt, E. High-Resolution Steady-State Cerebral Blood Volume Maps in Patients with Central Nervous System Neoplasms Using Ferumoxytol, a Superparamagnetic Iron Oxide Nanoparticle. *Journal of Cerebral Blood Flow & Metabolism* **33**, 780–786 (2013).

[17] Brown, T., Small, S., Hua, F. & Moreno, H. Longitudinal mapping of mouse cerebral blood volume with MRI. *NMR in Biomedicine* **19**, 535–543 (2006).

[18] Guo, J., Holdsworth, S., Fan, A., Lebel, M., Zun, Z., Shankaranarayanan, A. & Zaharchuk, G. Comparing accuracy and reproducibility of sequential and Hadamard-encoded multidelay pseudocontinuous arterial spin labeling for measuring cerebral blood flow and arterial transit time in healthy subjects: A simulation and in vivo study. *Journal of Magnetic Resonance Imaging* **47**, 1119–1132 (2017).

[19] Chou, N., Wu, J., Bingren, J. B., Qiu, A. & Chuang, K. Robust Automatic Rodent Brain Extraction Using 3-D Pulse-Coupled Neural Networks (PCNN). *IEEE Transactions on Image Processing* **20**, 2554–2564 (2011).

[20] Reuter, M., Schmansky, N., Rosas, H. & Fischla, B. Within-subject template estimation for unbiased longitudinal image analysis. *NeuroImage* **61**, 1402–1418 (2012).

[21] Avants, B., Tustison, N., Song, G., Cook, P., Klein, A. & Gee, J. A reproducible evaluation of ANTs similarity metric performance in brain image registration. *NeuroImage* **54**, 2033–2044 (2011).

[22] Kjølby, B. F., Østergaard, L. & Kiselev, V. G. Theoretical model of intravascular paramagnetic tracers effect on tissue relaxation. *Magnetic Resonance in Medicine* **56**, 187–197 (2006).

[23] Meier, P. & Zierler, K. L. On the Theory of the Indicator-Dilution Method for Measurement of Blood Flow and Volume. *Journal of Applied Physiology* **6**, 731–744 (1954).

[24] Østergaard, L., Weisskoff, R., Chesler, D., Gyldensted, C. & Rosen, B. High resolution measurement of cerebral blood flow using intravascular tracer bolus passages. Part I: Mathematical approach and statistical analysis, *Magnetic Resonance in Medicine*. **36**, 715–725 (1996).

[25] Willats, L. & Calamante, F. The 39 steps: evading error and deciphering the secrets for accurate dynamic susceptibility contrast MRI. *NMR in Biomedicine* **26**, 913-31 (2013)

[26] Rempp, K. A. et al. Quantification of regional cerebral blood flow and volume with dynamic susceptibility contrast-enhanced MR imaging. *Radiology* 193, 637–641 (1994).

[27] Neska-Matuszewska, M., Bladowska, J., Sąsiadek, M. & Zimny, A. Differentiation of glioblastoma multiforme, metastases and primary central nervous system lymphomas using multiparametric perfusion and diffusion MR imaging of a tumor core and a peritumoral zone-Searching for a practical approach. *PLoS ONE* **13**, e0191341 (2018).

[28] Mehta, A., Awah, C. U. & Sonabend, A. M. Topoisomerase II Poisons for Glioblastoma; Existing Challenges and Opportunities to Personalize Therapy. *Frontiers in Neurology*. **9**, (2018).